Infrared Physics and Technology 109 (2020) 103388

Contents lists available at ScienceDirect

Infrared Physics & Technology

journal homepage: www.elsevier.com/locate/infrared

Direct comparison of the results of arsenic ion implantation in *n*– and *p*–type $Hg_{0.8}Cd_{0.2}Te$

I.I. Izhnin[a,b], K.D. Mynbaev[c,*], Z. Swiatek[d], J. Morgiel[d], A.V. Voitsekhovskii[b], A.G. Korotaev[b], V.S. Varavin[e], S.A. Dvoretsky[b,e], D.V. Marin[e], M.V. Yakushev[e], O.I. Fitsych[f], O.Yu. Bonchyk[g], H.V. Savytskyy[g]

[a] Scientific Research Company "Electron-Carat", Lviv 79031, Ukraine
[b] National Research Tomsk State University, Tomsk 634050, Russia
[c] ITMO University, St.-Petersburg 197101, Russia
[d] Institute of Metallurgy and Materials Science PAN, Krakow 30-059, Poland
[e] A V Rzhanov Institute of Semiconductor Physics of SB RAS, Novosibirsk 630090, Russia
[f] P Sahaidachny National Army Academy, Lviv 79012, Ukraine
[g] Pidstryhach Institute for Applied Problems of Mechanics and Mathematics NASU, Lviv 79060, Ukraine

A R T I C L E I N F O

Keywords:
HgCdTe
Arsenic implantation
Defects

A B S T R A C T

Optical reflectance in the visible wavelength range, transmission electron microscopy, and the Hall-effect measurements with mobility spectrum analysis have been used for the direct comparison of the results of arsenic ion implantation in samples with *n*– and *p*–type conductivity fabricated on the basis of a $Hg_{1-x}Cd_xTe$ film with $x = 0.22$ grown by molecular beam epitaxy on a Si substrate. Optical reflectance studies showed that the effect of ion implantation on the properties of the surface was very similar in *n*– and *p*–type material. Transmission electron microscopy showed that defect patterns were also similar in *n*– and *p*–type samples in terms of the thicknesses of implantation-damaged layers and types of defects formed. Electrical studies demonstrated that low- and mid-mobility electrons induced by the implantation in *n*– and *p*–type material had similar average concentration and mobility. It was concluded that the nature of donor defects that produced these electrons was the same in *n*– and *p*–type HgCdTe, and it was suggested that the defects in question were interstitial mercury atoms captured by dislocation loops and by quasi-point defects formed as a result of implantation.

1. Introduction

For the last fifty years, HgCdTe (MCT) solid solutions have remained the basic material for photodetectors operating in the long- and middle-wavelength infrared ranges [1–3]. One of the most popular methods used for the fabrication of MCT-based photodiodes is ion implantation, and the recent studies of the effect of the implantation on MCT properties involved those of the influence of, e.g., the type of the implanted specie [4], the implantation dose, energy and temperature [5], the profile of implanted ions [6], the type of surface passivation layer [7], etc. Ion implantation serves as a basis for both the extrinsic 'p^+–on–*n*' (typically, arsenic implantation) and intrinsic 'n^+–on–*p*' (typically, boron implantation) photodiode technologies. Of these, 'p^+–on–*n*' technology currently attracts much attention due to the fact that it allows for reducing photodiode dark current, and thus, for increasing the operating temperature of the device or its cut-off wavelength [8,9]. The 'p^+–on–*n*' architecture can be implemented with heterojunction technology [10,11], but the success of *in situ* fabrication of 'p^+–*n*' junctions is still limited because of challenges related to achieving high hole concentration in p^+–type layer and strong Hg/Cd interdiffusion during high-temperature arsenic activation annealing [3]. Thus, implantation remains a solid option for this architecture. To fabricate p^+–on-*n* photodiodes with this technology, implantation is performed into a 'base' *n*–type layer doped with indium to (1–5)·10^{15} cm^{-3} [12,13]. The doping ensures that the properties of the 'base' during post-implantation annealing, which is performed for the activation of implanted ions and healing of implantation damage, are kept stable. At that, high electrical conductivity of the indium-doped 'base' *n*–layer hinders electrical studies of the *p*–type layer formed after the annealing due to the large difference in electron and hole mobility in MCT. Thus, the effect of the arsenic implantation on the properties of MCT is typically studied after implantation into *p*–type material [14]. This approach

* Corresponding author at: Kronverksky 49-A, Saint-Petersburg 197101, Russia.
E-mail address: mynkad@mail.ioffe.ru (K.D. Mynbaev).

https://doi.org/10.1016/j.infrared.2020.103388
Received 10 April 2020; Received in revised form 1 June 2020; Accepted 1 June 2020
Available online 03 June 2020
1350-4495/ © 2020 Elsevier B.V. All rights reserved.

presumes that formation of implantation-induced defects, including electrically active ones, proceeds similarly in the 'base' layers with *p*– and *n*–type conductivity. To the best of our knowledge, no direct proof to this fact has been given yet with the exception of very limited data obtained with single-field Hall-effect measurements on MCT epitaxial films implanted with nitrogen [15]. In this work, we performed a direct comparison of the effect of arsenic implantation on the properties of *n*– and *p*–type samples made from the same epitaxial $Hg_{0.8}Cd_{0.2}Te$ film, – in relation to their surface, structural, and electrical properties.

2. Material and methods

The 9.1 μm-thick film was grown at Rzhanov Institute of Semiconductor Physics (Novosibirsk, Russia) by molecular beam epitaxy (MBE) on a (0 1 3)CdTe/ZnTe/Si substrate with the growth cycle controlled *in situ* by means of an ellipsometer [16]. The 'absorber' layer of the film with CdTe molar fraction (composition) $x_a \approx 0.22$ was *in situ* covered with ~0.4 μm-thick graded-gap protective layer with $x_v \approx 0.46$ at the surface. The film was doped with indium during the growth with calculated concentration in the absorber layer $6.0 \cdot 10^{15}$ cm^{-3}. The indium concentration was gradually increasing in the graded-gap surface layer and reached $1.6 \cdot 10^{16}$ cm^{-3} at its surface.

Indium doping provided *n*-type conductivity of the as-grown film. A piece cut from the film after the growth was subjected to thermal annealing (220 ^{0}C, 24 h) in helium atmosphere at low mercury pressure. As a result of the annealing, a *p*–type sample was fabricated with hole conductivity resulting from the presence of mercury vacancies, intrinsic acceptors in MCT.

Both *n*– and *p*–type samples were implanted in one implantation cycle with As^+ ions with the energy 190 keV and fluence 10^{14} cm^{-2} using IMC200 (Ion Beam Services, France) machine.

The surface characterization was performed with optical reflectance measurements performed at the temperature T = 295 K in 300–750 nm wavelength range with 0.2 nm step with the use of Shimadzu UV-3600 (Japan) spectrophotometer with 5 mm diaphragm.

The microstructure of the implanted material was studied with Transmission Electron Microscopy (TEM) in bright-field (BF) and high-resolution (HRTEM) modes with the use of Tecnai G2 F20, FEI Company microscope. Thin foils were prepared using FEI Quanta 200 dual-beam focused-ion (Ga^+) beam machine equipped with an OmniprobeTM lift-out system.

The electrical properties of the material were studied by measuring the magnetic field B dependences of the Hall coefficient R_H and the conductivity σ in the B = 0.01–1.5 T range at T = 77 K. The obtained data were analyzed with the use of the discrete mobility spectrum analysis (DMSA) [14]; this technique allows for determining the number of carrier species and their parameters: concentration, mobility and partial conductivity. In particular, the analysis of the as-grown film (sample *1*, *n*-type) showed that its conductivity was dominated by high-mobility electrons of the 'absorber' layer (majority carriers) with average (reduced to the total thickness of the film) concentration $3.9 \cdot 10^{15}$ cm^{-3}; mobility, 87500 cm^2/(V·s); and average partial conductivity 54.6 (Ohm·cm)$^{-1}$ with directly measured total conductivity equaling 56.6 (Ohm·cm)$^{-1}$. Electrons with mid-mobility were also detected; these are typical of the structures grown by the MBE method considered and are located in the transitional layer at the film/buffer layer interface [17,18]. Their parameters were as follows: average concentration $4.93 \cdot 10^{14}$ cm^{-3} (sheet concentration N_{sh} = $4.4 \cdot 10^{11}$ cm^{-2}); mobility, 12200 cm^2/(V·s); average partial conductivity, 0.96 (Ohm·cm)$^{-1}$. The total partial conductivity provided by holes was 0.1%, so their parameters could not be appropriately resolved.

In *p*–type sample *2* the conductivity was dominated by heavy holes of the 'absorber' layer (majority carriers) with average concentration $5.07 \cdot 10^{15}$ cm^{-3}, mobility 384 cm^2/(V·s), and average partial conductivity 0.31 (Ohm·cm)$^{-1}$ with directly measured total conductivity equaling 0.325 (Ohm·cm)$^{-1}$. Light holes also contributed to the conductivity, their parameters were as follows: concentration $4.93 \cdot 10^{14}$ cm^{-3}; mobility, 12600 cm^2/(V·s), partial conductivity, 0.009 (Ohm·cm)$^{-1}$. The transitional-layer mid-mobility electrons were also present in this sample, they had average concentration $1.77 \cdot 10^{12}$ cm^{-3}, mobility, 13000 cm^2/(V·s), and average partial conductivity, 0.004 (Ohm·cm)$^{-1}$.

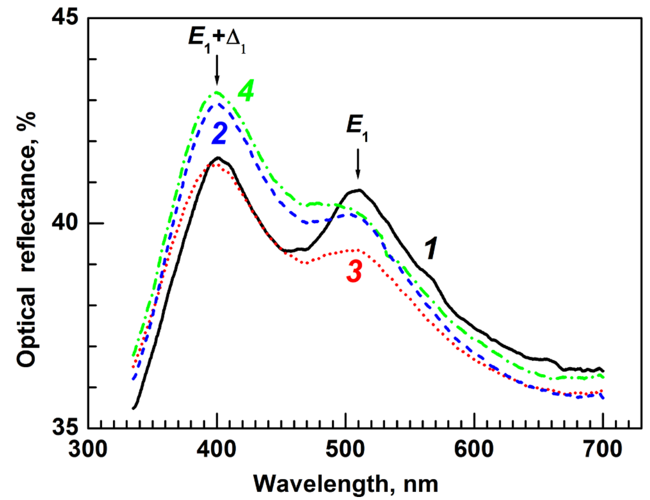

Fig. 1. Optical reflectance spectra of the studied samples: *1* (*n*–type, not implanted); *2* (*p*–type, not implanted); *3* (*n*–type, implanted); *4* (*p*–type, implanted).

The high-mobility electrons (minority carriers) were also present in sample *2*. Their partial contribution to the conductivity was the lowest one and the parameters were as follows: average concentration, $6 \cdot 10^{10}$ cm^{-3}, mobility, 83100 cm^2/(V·s), average partial conductivity, 0.001 (Ohm·cm)$^{-1}$. This mobility value appeared to be in good agreement with that in sample *1*, which confirmed the validity of the DMSA procedures performed.

3. Results and discussion

3.1. Optical reflectance studies

Fig. 1 shows optical reflectance spectra of the studied samples. The spectra contained a typical doublet of the peaks E_1 and $E_1 + \Delta_1$, which originated in transitions $\Lambda_{4,5} \to \Lambda_6$ and $\Lambda_6 \to \Lambda_6$, respectively [19]. To assess the structural perfection of the surface of the samples, we used the value of "peak sharpness" $Q = \Delta R/R_1$, where ΔR is the value of the 'dip' between the peaks and R_1 is the reflectance in the maximum of the peak E_1 [20]. The chemical composition on the surface was determined on the basis of the position of peak E_1.

The analysis of the transformation of values of Q showed that the crystalline perfection of the surface layer of sample *2* (Q = 2.68) was much lower than that of sample *1* (Q = 4.59). This tentatively could be considered to be a result of the evaporation of mercury from the surface of the material, as the exact aim of the annealing used to obtain sample *2* was the generation of mercury vacancies. The evaporation also explained the substantial ($\Delta x_v \approx 0.04$) increase in the composition at the surface after the annealing; this result of heating is typical of Hg-related compounds irrespective of the source of the heat (for the most recent studies on this topic, see, e.g., [21]). Ion implantation resulted in significant decrease in the value of Q for both samples; in sample *3* Q equaled 2.67, in sample *4*, 1.05. According to the results of the TEM studies, which are given below, the origin of this effect was the formation of extended structural defects in the sub-surface layers of the samples.

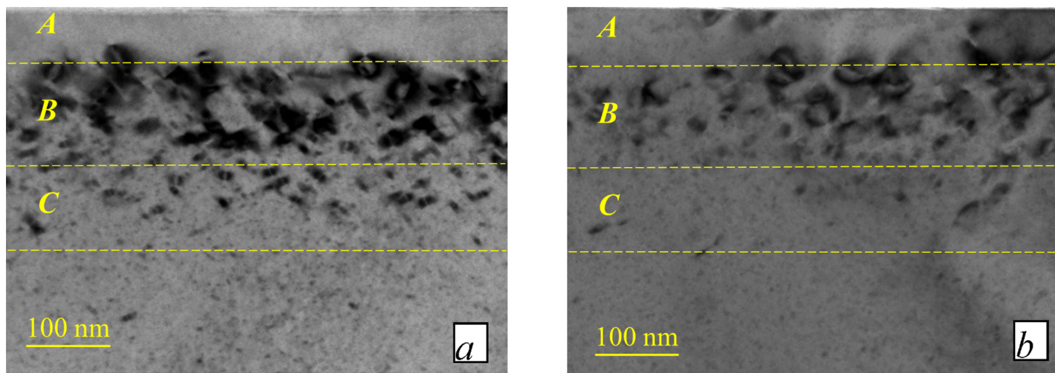

Fig. 2. BF-TEM images of the cross-sectional views of samples *3* (*a*) and *4* (*b*). The material was implanted with arsenic with ion energy 190 keV and ion fluence 10^{14} cm^{-2}.

3.2. Transmission electron microscopy studies

Fig. 2 shows TEM images of the cross-sectional views of the implanted samples. The defect patterns observed in the two images were very similar and appeared to be typical of the arsenic-implanted MCT [22–24]. First, the whole implantation-damaged layer extended to a considerable depth, almost to 330 nm. Secondly, the layer could be divided into three characteristic sub-layers. The top sub-layers *A* had thicknesses ~70 nm in both samples and possessed a low density of structural defects. Similar layers were first observed by Lobre *et al.* [24], and their formation was related to the partial re-structuring (recombination) of the implantation-induced defects that took place during the implantation. This is a characteristic feature of materials with the strong ionic nature of the chemical bonds [24]. The sub-layers *A* were followed by sub-layers *B*, which contained 'large' structural defects; the densities of these defects were high. The thicknesses of the sub-layers *B* equaled ~120 nm in both samples. The sub-layers *B* were followed by ~100 nm-thick sub-layers *C*, which contained 'small' extended defects; the densities of these defects were low. These sub-layers were followed by the layers containing quasi-point defects, which could not be visualized in BF-TEM mode and appeared in the images as a uniform background.

More detailed information on the specific types of defects formed in the implanted material was obtained in the course of HRTEM studies. The structural defects produced by ion implantation in *n*–type sample *3* were analyzed in detail by Bonchyk et al. [22], so in this work we focused on the defects in *p*–type sample *4*. Fig. 3 shows HRTEM data obtained from an area located in sub-layer *A*. The results of the BF-TEM study shown above suggested that this sub-layer contained isolated structural defects with low density. Indeed, in Fig. 3 one can observe isolated vacancy-type dislocation loops P_2 (3 nm in size, see Fig. 3(b)) and P_3 (5 nm) against the background of almost perfect crystalline structure. A stacking fault and some single dislocations are seen in the image, but the general defect density is indeed low.

The damage produced by ion implantation was most clearly seen in the sub-layer *B*. It contained high density of large extended structural defects along with defect complexes and agglomerates. The most typical defects were large dislocation loops, other defects were single dislocations, stacking faults and lattice deformations. Fig. 4 shows an example of defect area in the sub-layer *B*. Dark grey areas in Fig. 4(a) show spots with considerable lattice disorder. IFFT images in Fig. 4(*b,c*) show vacancy- (P_4, P_5) and interstitial-type (P_6) dislocation loops. These loops were large in size: for P_4, the size of the loop was ~10 nm; for P_5, 12 nm; for P_6, ~15 nm. The loops were accompanied by numerous dislocations and lattice deformations.

The defects in the sub-layer *C* were smaller in size than those in the sub-layer *B*. This is illustrated in Fig. 5, where an image of a defect area in the sub-layer *C* is shown. Only one dislocation loop P_7 with 7 nm in size is visible in Fig. 5(b), along with few single dislocations. In general, the defect patterns formed by the implantation in MCT with *p*–type conductivity (Figs. 3–5) and *n*–type conductivity (as presented in Ref. [22]) appeared to be very similar.

Fig. 6 shows simulated profiles of arsenic ions and displaced atoms (vacancies) in MCT for ion implantation of arsenic with energy 190 keV

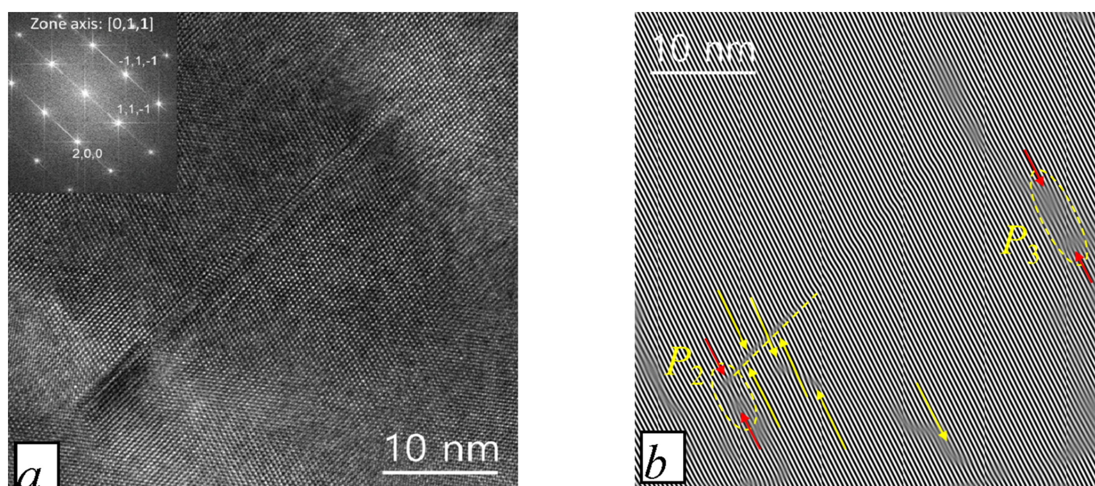

Fig. 3. HRTEM image of an area in the sub-layer *A* of sample *4* with inset showing its fast Fourier transform (FFT) image (*a*), and corresponding inverse FFT (IFFT) image (*b*). Red arrows and dashed ovals in image (*b*) mark dislocation loops; yellow arrows, single dislocations; dashed line, a stacking fault. (For interpretation of the references to colour in this figure legend, the reader is referred to the web version of this article.)

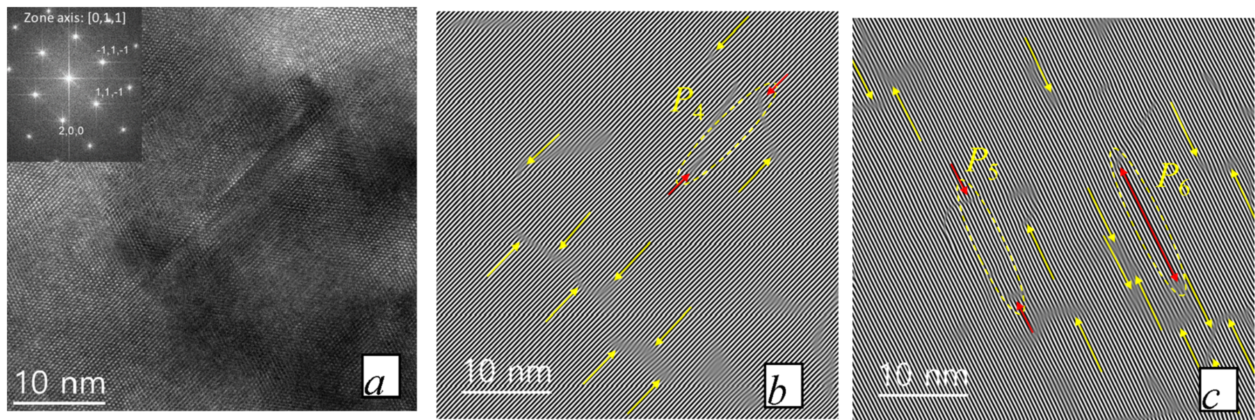

Fig. 4. HRTEM image of an area of the sub-layer *B* of sample *4* with inset showing its FFT image (*a*), and corresponding IFFT images (*b,c*). Red arrows and dashed ovals in images (*b*) and (*c*) mark dislocation loops; yellow arrows, single dislocations. (For interpretation of the references to colour in this figure legend, the reader is referred to the web version of this article.)

and fluence 10^{14} cm^{-2}. The simulation was performed with the use of SRIM-2013 free software [25]. The profiles are plotted against the background of the BF-TEM images of the cross-sections of the samples.

The simulated value of the projected ion range R_p equaled 93 nm. As follows from Fig. 6, the position of R_p corresponded to the upper parts of the sub-layers *B*, while the whole defect layer extended much deeper. According to the simulated profiles of generated vacancies, the areas with the highest concentration of implantation-induced defects should have formed within the sub-layers *A*. Thus, according to the results of simulations, the surface layers with low defect density could be expected to be much thinner than those observed experimentally. The actual defect pattern in the TEM images can be explained only by the recombination of structural defects and partial restoration of the crystalline structure that proceeded during the implantation, as mentioned above.

The SRIM software does not allow for considering the conductivity type of the material under implantation, thus the profiles of the vacancies in Fig. 6 were the same in *n*– and *p*–type samples. It could be expected that the presence of intrinsic vacancies in the vacancy-doped *p*–type sample could somehow affect the defect formation in the damaged area (e.g., via favoring the formation of vacancy-type dislocation loops), but no effect of this kind was observed. Most likely, the concentration of the vacancies in the initial sample was too low as compared to that of the vacancies generated with the implantation.

Studies of the profiles of structural defects in implanted MCT (see, e.g., Ref. [24]) for various energies of the arsenic ions showed that extended structural defects spread to the depths approx. 1.8–2 larger than the R_p (see also Ref. [26]). In the crystals with prevailing covalent bonding, the maximum of the concentration of implantation-induced extended defects is located close to R_p. In MCT, which is a material with the prevailing ionic bonding, the maximum is located much deeper than R_p. Once more, this is indicative of the fact that primary implantation-induced defects in MCT are undergoing transformation already during the implantation with their recombination proceeding much easier than that in the covalent-bonded crystals.

3.3. Electrical studies

Fig. 7 shows primary mobility spectrum envelopes (MSE) of the studied samples. These MSEs were calculated using the classic MSA algorithm developed by Beck and Anderson [27]. As mentioned above, the analysis of the MSEs showed that in the initial *n*–type sample *1* the conductivity was dominated by the high-mobility electrons (curve *1*), while in *p*–type sample *2* it was dominated by the heavy and light holes (curve *2*). After ion implantation (curves *3* and *4*) the shapes of the MSEs were substantially changed, reflecting the changes in the types of the carriers that were dominating the conductivity.

The results of the DMSA of the $R_H(B)$ and $\sigma(B)$ dependences for the

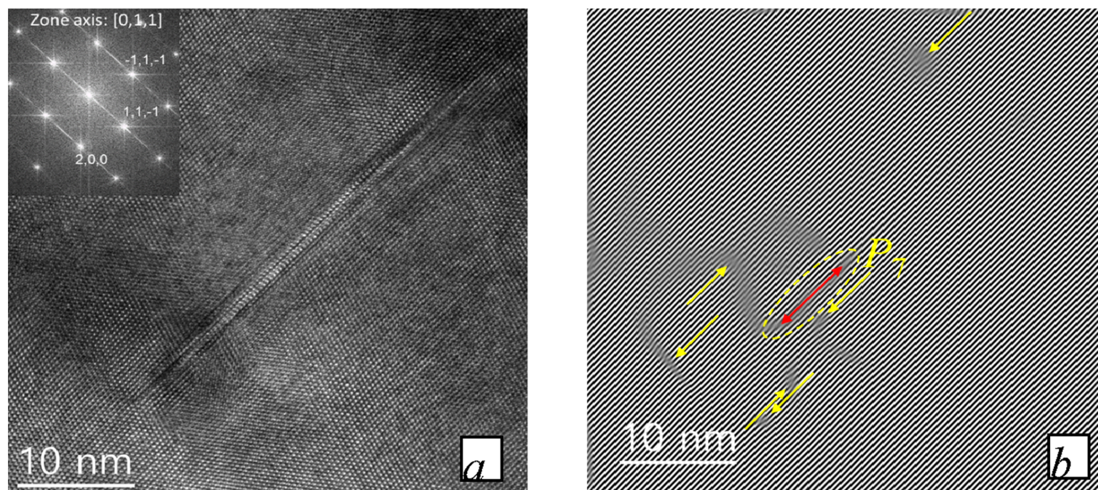

Fig. 5. HRTEM image of an area of the sub-layer *C* of sample *4* with inset showing its FFT image (*a*), and corresponding IFFT image (*b*). Red arrow and dashed ovals in image (*b*) mark dislocation loops; yellow arrows, single dislocations. (For interpretation of the references to colour in this figure legend, the reader is referred to the web version of this article.)

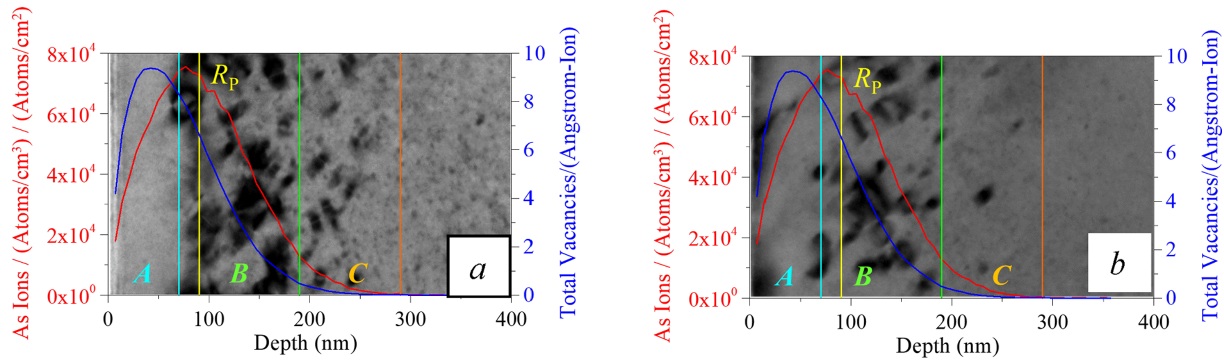

Fig. 6. Simulated profiles of arsenic ions and produced vacancies in MCT for arsenic implantation with energy 190 keV and fluence 10^{14} cm^{-2} plotted against the background of BF-TEM images of the cross-sections of samples *3* (*a*) and *4* (*b*).

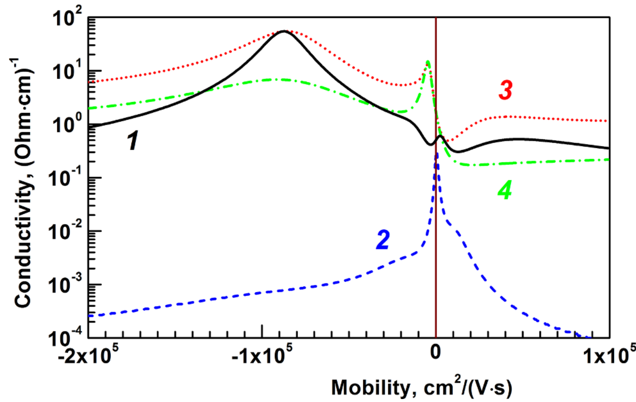

Fig. 7. Primary mobility spectrum envelopes for samples *1, 2, 3* and *4* (curves *1*, *2*, *3* and *4*, respectively). The negative part of the mobility axis was introduced for the clarity only.

implanted samples *3* and *4* are shown in Fig. 8. Images (*a*) and (*b*) show the MSEs, while images (*c*) and (*d*) show the corresponding experimental and calculated, as a result of the performed analysis, $R_H(B)$ and resistivity ρ(*B*) dependences. In sample *4* with initial *p*–type conductivity (Fig. 8(b)), ion implantation resulted in the formation of an n^+–*n*–*p* structure. Similar structures were formed in *p*–type MCT with $x_a \approx 0.2$ after arsenic implantation with fluences in 10^{12}–10^{15} cm^{-2} range [14,28]. In these structures, the *p*–type region represents the 'base' that was not affected by the implantation, while the n^+–*n*–region forms as its result. In sample *4*, the dominating contribution to the conductivity was that by the low-mobility (4650 cm^2/(V·s), average concentration 2.00·10^{16} cm^{-3}) electrons, which provided average partial conductivity 14.9 (Ohm·cm)$^{-1}$ with the total measured conductivity equaling 24.46 (Ohm·cm)$^{-1}$. This can be seen in Fig. 8(b) (curve *1*), where the corresponding mobility peak is clearly dominating. These carriers originate in implantation-induced structural defects and are localized in the n^+–region, which is the layer containing extended structural defects, such as dislocation loops (Fig. 2, see also Refs. [14,28]). The donors producing these electrons are mercury atoms that were displaced by the implantation, became mobile interstitials Hg_I, and got captured by dislocation loops. The next contribution to the conductivity was that by the high-mobility (99600 cm^2/(V·s), average concentration 4.15·10^{14} cm^{-3}) electrons. Their average partial conductivity equaled 6.61 (Ohm·cm)$^{-1}$. These electrons are known to originate in the residual/introduced donors that determine the conductivity after the atoms of Hg_I had diffused into the crystal and annihilated with mercury vacancies that defined the *p*-type conductivity of the 'base' before the implantation [28,29]. Also, electrons with the mid-mobility (19400 cm^2/(V·s), average concentration 5.5·10^{14} cm^{-3}) were found in sample *4*. Their average partial conductivity equaled 1.71 (Ohm·cm)$^{-1}$. These electrons are also located in the n^+–region, as carriers with these parameters were absent in the initial sample. These electrons originated in the donor complexes that Hg_I atoms formed with quasi-point defects [14]. A similar assortment of carriers with three types of electrons possessing low-, intermediate- and high mobility, respectively, was observed in boron-implanted *p*–type MCT samples [30].

As mentioned above, in ion-implanted *n*–type MCT samples, the contribution to conductivity by the donor centers formed as a result of implantation is 'masked' by the high conductivity of the *n*-type base, especially if the 'base' was doped with a donor (indium). This makes it challenging to determine the partial conductivity due to the defects induced by the implantation and to separate this conductivity from that due to the electrons of the *n*–base. This was exactly the case for sample *3* (Fig. 8(a)). The implantation resulted in the formation of the n^+–*n*–structure, where the *n*–region represented a part of the 'base' that was not affected by the implantation, while the n^+–region was its direct result. The dominating contribution to the conductivity of the structure was that by the high-mobility electrons of the *n*-region. The average partial conductivity provided by these electrons equaled 55.0 (Ohm·cm)$^{-1}$ (which value agreed well with the conductivity in as-grown sample *1*, 56.0 (Ohm·cm)$^{-1}$), with the total conductivity of the structure equaling 74.5 (Ohm·cm)$^{-1}$. These electrons showed off in the primary MSE (Fig. 8(a), curve *1*) in the mobility peak at 85700 cm^2/(V·s). Their average concentration equaled 4.01·10^{15} cm^{-3}, and as the thickness of the n^+–layer was small, this value appeared to be very close to the average electron concentration in sample *1*, 3.9·10^{15} cm^{-3}. These electrons originate in the residual/introduced donors of the *n*–base, in our case, indium atoms.

The next contribution to conductivity was that of the low-mobility electrons that provided partial conductivity 11.7 (Ohm·cm)$^{-1}$. Indeed, this value was much smaller than that of the 'base' layer, yet the primary MSE (Fig. 8(a)) still showed a sharp peak at mobility value 3590 cm^2/(V·s), which allowed for determining their average concentration as 2.03·10^{16} cm^{-3}. It can be suggested that these electrons, similar to those in sample *4* (which also had electron concentration ~2·10^{16} cm^{-3}), originated in Hg_I atoms captured by dislocation loops [14,28]. Thus, the process of the formation of these donor defects seemed to be in no way affected by the conductivity of the material, be it *n*–type or *p*–type.

Sample *3* also contained the mid-mobility (12000 cm^2/(V·s)) electrons with the average concentration 3.1·10^{15} cm^{-3} and the average partial conductivity 5.98 (Ohm·cm)$^{-1}$. The concentration of these electrons in sample *3* was almost an order of magnitude higher than that in sample *4*. Most likely, this was due to the fact that in sample *3* there were two sorts of electrons with similar mobility values, with one sort being electrons of the *n*–'base' (to be exact, the electrons of the transitional layer near the CdTe buffer layer), and the other one originating in Hg_I atoms captured by quasi-point defects induced by the implantation.

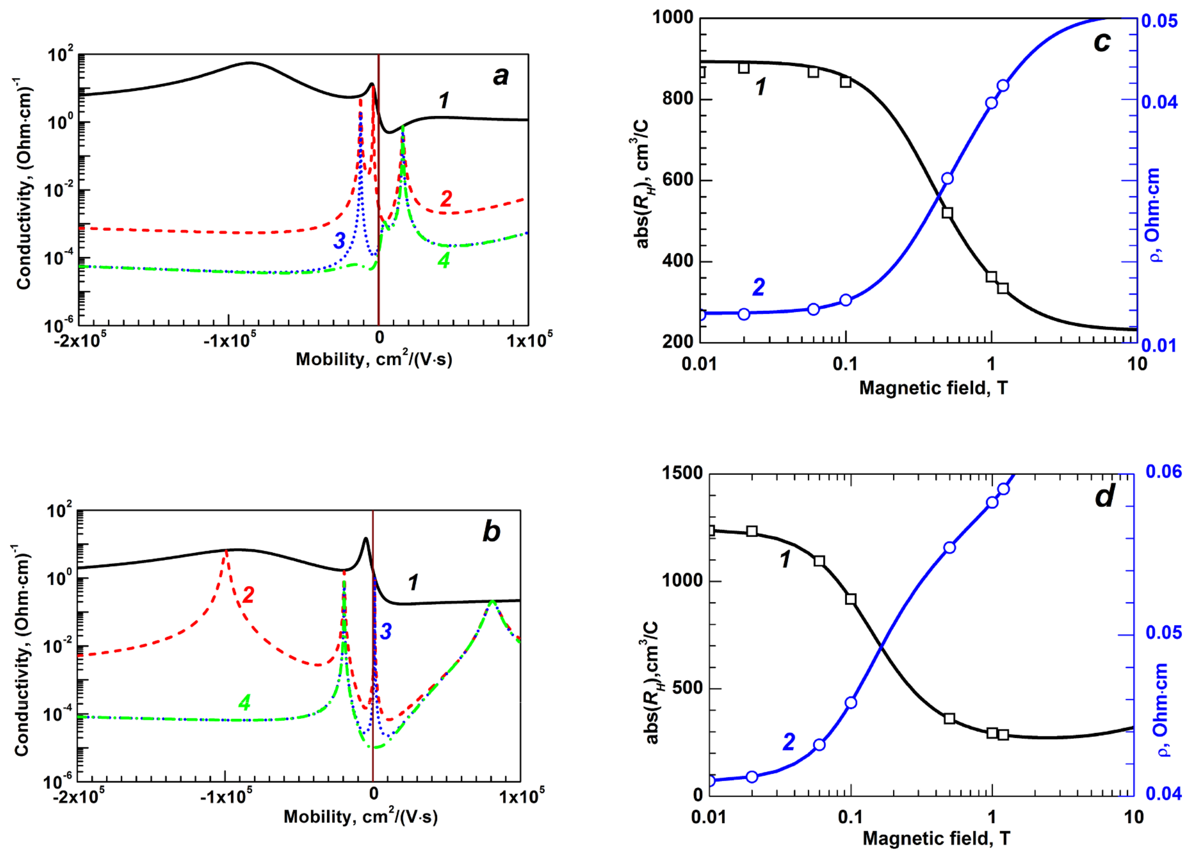

Fig. 8. Mobility spectrum envelopes obtained with the use of DMSA for samples *3* (*a*) and *4* (*b*), and corresponding experimental (points) and calculated (lines) $R_H(B)$ (*1*, $R_H < 0$) and ρ(*B*) (*2*) dependences (*c*, *d*). Curves in graphs (*a*) and (*b*) show envelopes: *1*, primary envelopes; *2*, *3* and *4*, envelopes after the first, the second and the third discretization steps, respectively. A good agreement between the corresponding experimental and calculated $R_H(B)$ and ρ(*B*) dependences in graphs (*c*) and (*d*) confirms the validity of the analysis performed.

4. Conclusion

Optical reflectance, TEM and electrical studies allowed us to perform a comprehensive direct comparison of the effect of arsenic ion implantation on the properties of *n*– and *p*–type $Hg_{0.78}Cd_{0.22}Te$ samples fabricated from the same molecular beam epitaxy-grown film. It appeared that the annealing used for converting the conductivity type from *n*– to *p*– via generation of mercury vacancies substantially disrupted the crystalline perfection of the MCT surface. Still, the effect of the implantation on the structural quality of the surface appeared to be very similar in *n*– and *p*–type material. BF–TEM and HRTEM studies showed that the defect layers produced by the implantation were also similar in *n*– and *p*–type samples in terms of the thicknesses of the damaged layers and the types of the induced defects. Electrical studies demonstrated that low- and mid-mobility electrons induced by the implantation in *n*– and *p*–type material also had very similar parameters (average concentration and mobility). It was concluded that the nature of donor defects that produced these electrons was the same in both types of samples, supposedly representing interstitial mercury atoms captured by dislocation loops and by quasi-point defects, with both types of defects formed as a result of the implantation damage.

Declaration of Competing Interest

The authors declare that they have no known competing financial interests or personal relationships that could have appeared to influence the work reported in this paper.

References

[1] A. Rogalski, HgCdTe photodetectors, Chapter 7, in: E. Tournié, L. Cerutti (Eds.), Mid-Infrared Optoelectronics, Woodhead Publishing (Elsevier), Duxford, Cambridge, Kindlington, 2020, pp. 235–335.
[2] R.K. Bhan, V. Dhar, Recent infrared detector technologies, applications, trends and development of HgCdTe based cooled infrared focal plane arrays and their characterization, Opto-Electron. Review 27 (2019) 174–193, https://doi.org/10.1016/j.opelre.2019.04.004.
[3] W. Lei, J. Antoszewski, L. Faraone, Progress, challenges, and opportunities for HgCdTe infrared materials and detectors, Appl. Phys. Rev. 2 (2015) 041303, https://doi.org/10.1063/1.4936577.
[4] C. Lobre, P.H. Jouneau, L. Mollard, P. Ballet, Characterization of the microstructure of HgCdTe with *p*-type doping, J. Electron. Mater. 43 (2014) 2908–2914, https://doi.org/10.1007/s11664-014-3147-9.
[5] N. Talipov, A.V. Voitsekhovskii, Ion implantation in narrow-gap $Cd_xHg_{1-x}Te$ solid solutions, Russ. Phys. J. 61 (2018) 1005–1023, https://doi.org/10.1007/s11182-018-1490-7.
[6] A.L. Cui, L.F. Liu, C.H. Sun, R.J. Ding, L. He, Z.H. Ye, Analysis of dark current generated by long-wave infrared HgCdTe photodiodes with different implantation shapes, Infr. Phys. Technol. 103 (2019) 103036, https://doi.org/10.1016/j.infrared.2019.103036.
[7] C.Z. Shi, C. Lin, Y.F. Wei, L. Chen, M.X. Zhu, Barrier layer induced channelling effect of As ion implantation in HgCdTe and its influences on electrical properties of p-n junctions, Appl. Opt. 55 (2016) D101–D105, https://doi.org/10.1364/AO.55.00D101.
[8] A.P. Kovchavtsev, A.A. Guzev, A.V. Tsarenko, Z.V. Panova, M.V. Yakushev, D.V. Marin, V.S. Varavin, V.V. Vasilyev, S.A. Dvoretsky, I.V. Sabinina, Y.G. Sidorov, The reverse current temperature dependences of SWIR CdHgTe "*p*-on-*n*" and "*n*-on-*p*" junctions, Infr. Phys. Technol. 73 (2015) 312–315, https://doi.org/10.1016/j.infrared.2015.09.026.
[9] A. Yeche, F. Boulard, O. Gravrand, Development of electron beam induced current characterization of HgCdTe based photodiodes, J. Electron. Mater. 48 (2019) 6045–6052, https://doi.org/10.1007/s11664-019-07140-7.
[10] O. Gravrand, P. Ballet, J. Baylet, N. Baier, HgCdTe p-on-n Focal-Plane Array Fabrication Using Arsenic Incorporation During MBE Growth, J. Electron. Mater. 38 (2009) 1684–1689, https://doi.org/10.1007/s11664-009-0794-3.
[11] E.P.G. Smith, G.M. Venzor, Y. Petraitis, M.V. Liguori, A.R. Levy, C.K. Rabkin,

J.M. Peterson, M. Reddy, S.M. Johnson, J.W. Bangs, Fabrication and characterization of small unit-cell molecular beam epitaxy grown HgCdTe-on-Si mid-wavelength infrared detectors, J. Electron. Mater. 36 (2007) 1045–1051, https://doi.org/10.1007/s11664-007-0169-6.
[12] L. Mollard, G. Bourgeois, C. Lobre, S. Gout, S. Viollet-Bosson, N. Baier, G. Destefanis, O. Gravrand, J.P. Barnes, F. Milesi, A. Kerlain, L. Rubaldo, A. Manissadjian, P-on-n HgCdTe infrared focal-plane arrays: from short-wave to very-long-wave infrared, J. Electron. Mater. 43 (2014) 802–807, https://doi.org/10.1007/s11664-013-2809-3.
[13] C.A. Billman, L.A. Almeida, P. Smith, J.M. Arias, A. Chen, D. Lee, E.C. Piquette, EC The effects of microvoid defects on MWIR HgCdTe-based diodes, J. Electron. Mater. 40 (2011) 1693–1698, https://doi.org/10.1007/s11664-011-1658-1.
[14] I.I. Izhnin, K.D. Mynbaev, A.V. Voitsekhovsky, A.G. Korotaev, I.I. Syvorotka, O.I. Fitsych, V.S. Varavin, S.A. Dvoretsky, N.N. Mikhailov, V.G. Remesnik, M.V. Yakushev, Z. Swiatek, J. Morgiel, O.Yu. Bonchyk, H.V. Savytskyy, Arsenic-ion implantation-induced defects in HgCdTe films studied with Hall-effect measurements and mobility spectrum analysis, Infr. Phys. Technol. 98 (2019) 230–235, https://doi.org/10.1016/j.infrared.2019.03.019.
[15] A.V. Voitsekhovskii, D.V. Grigor'ev, N.Kh Talipov, Ion implantation into heteroepitaxial $Cd_xHg_{1-x}Te$ grown by molecular-beam epitaxy, Russ. Phys. J. 51 (2008) 1001–1015, https://doi.org/10.1007/s11182-009-9142-6.
[16] M.V. Yakushev, D.V. Brunev, V.S. Varavin, V.V. Vasilyev, S.A. Dvoretskii, I.V. Marchishin, A.V. Predein, I.V. Sabinina, Yu.G. Sidorov, A.V. Sorochkin, HgCdTe heterostructures on Si(310) substrates for MWIR infrared photodetectors, Semiconductors 45 (2011) 385–391, https://doi.org/10.1134/S1063782611030250.
[17] V.S. Varavin, A.F. Kravchenko, Yu.G. Sidorov, A study of galvanomagnetic phenomena in MBE-grown n-Cd_xHg_{1-x} Te films, Semiconductors 35 (2001) 992–996, https://doi.org/10.1134/1.1403562.
[18] V.V. Bogoboyashchyy, S.A. Dvoretsky, I.I. Izhnin, N.N. Mikhailov, Yu.G. Sidorov, F.F. Sizov, V.S. Varavin, V.A. Yudenkov, Properties of MBE $Cd_xHg_{1-x}Te$/GaAs structures modified by ion-beam milling, Phys. Stat. Sol. (c) 1 (2004) 355–359, https://doi.org/10.1002/pssc.200303947.
[19] P. Koppel, Visible and ultraviolet reflectivity of $Hg_{1-x}Cd_xTe$, J. Appl. Phys. 57 (1985) 1705–1709, https://doi.org/10.1063/1.334441.
[20] S.A. Dvoretsky, N.N. Mikhailov, V.G. Remesnik, N.Kh. Talipov, Using reflection spectroscopy for assessing structural perfection of CdTe/GaAs films and $Cd_xHg_{1-x}Te$ crystals, Avtometriya 5 (1998) 73–77 (in Russian).
[21] W.W. Pan, Z.K. Zhang, W. Lei, Z. Liu, L. Faraone, A Raman spectroscopy study of MBE-grown $Hg_{1-x}Cd_xSe$ alloys grown on GaSb (211) by molecular beam epitaxy, Infr. Phys. Technol. 97 (2019) 365–370, https://doi.org/10.1016/j.infrared.2019.01.022.
[22] O.Yu. Bonchyk, H.V. Savytskyy, Z. Swiatek, J. Morgiel, I.I. Izhnin, A.V. Voitsekhovskii, A.G. Korotaev, K.D. Mynbaev, O.I. Fitsych, V.S. Varavin, S.A. Dvoretsky, D.V. Marin, M.V. Yakushev, Nano-size defects in arsenic-implanted HgCdTe films: a HRTEM study, Appl. Nanosci. 9 (2019) 725–730, https://doi.org/10.1007/s13204-018-0679-y.
[23] L. Mollard, G. Destefanis, G. Bourgeois, A. Ferron, N. Baier, O. Gravrand, J.P. Barnes, A.M. Papon, F. Milesi, A. Kerlain, L. Rubaldo, Status of *p*-on-*n* arsenic-implanted HgCdTe technologies, J. Electr. Mater. 40 (2011) 1830–1839, https://doi.org/10.1007/s11664-011-1692-z.
[24] C. Lobre, D. Jalabert, I. Vickridge, E. Briand, D. Benzeggouta, L. Mollard, P.H. Jouneau, P. Ballet, Quantitative damage depth profiles in arsenic implanted HgCdTe, Nucl. Instrum. Meth. B. 313 (2013) 76–80, https://doi.org/10.1016/j.nimb.2013.07.019.
[25] SRIM package: www.srim.org.
[26] G.L. Destefanis, Ion implantation in $Hg_{1-x}Cd_xTe$, Nucl. Instrum. Meth. 209 (210) (1983) 567–580, https://doi.org/10.1016/0167-5087(83)90854-2.
[27] W.A. Beck, J.R. Anderson, Determination of electrical transport properties using a novel magnetic field dependent Hall technique, J. Appl. Phys. 62 (1987) 541–553, https://doi.org/10.1063/1.339780.
[28] I.I. Izhnin, E.I. Fitsych, A.V. Voitsekhovskii, A.G. Korotaev, K.D. Mynbaev, V.S. Varavin, S.A. Dvoretsky, N.N. Mikhailov, M.V. Yakushev, O.Yu. Bonchyk, H.V. Savytskyy, Z. Świątek, Defects in arsenic-implanted p^+–n- and n^+–p-structures based on MBE-grown CdHgTe films, Russ. Phys. J. 60 (2018) 1752–1757, https://doi.org/10.1007/s11182-018-1278-9.
[29] L.O. Bubulac, Defects, diffusion and activation in ion implanted HgCdTe, J. Cryst. Growth 86 (1988) 723–734, https://doi.org/10.1016/0022-0248(90)90799-Q.
[30] G.A. Umana-Membreno, H. Kala, J. Antoszewski, Z.H. Ye, W.D. Hu, R.J. Ding, X.S. Chen, W. Lu, L. He, J.M. Dell, L. Faraone, Depth Profiling of Electronic Transport Parameters in n-on-p Boron-Ion-Implanted Vacancy-Doped HgCdTe, J. Electron. Mater. 42 (2013) 3108–3113, https://doi.org/10.1007/s11664-013-2659-z.